Proceedings of ASME Turbo Expo 2010: Power for Land, Sea and Air
June 14-18, 2010, Glasgow, UK

GT2010 - 23346

PREDICTION OF INGRESS THROUGH TURBINE RIM SEALS PART 1: EXTERNALLY-INDUCED INGRESS

J Michael Owen ensjmo@bath.ac.uk
Kunyuan Zhou* **Oliver Pountney**
Mike Wilson **Gary Lock**

Dept of Mechanical Engineering
University of Bath
Bath, BA2 7AY
United Kingdom

* Dept of Engineering Thermophysics
School of Jet Propulsion
Beihang University
Beijing, 100191 P.R.China

ABSTRACT

Rotationally-induced (RI) ingress is caused by the negative pressure (relative to the external air) inside the wheel-space of a gas turbine; this negative pressure, which is created by the rotating flow in the wheel-space, drives the ingestion of hot gas through the rim seals. *Externally-induced (EI) ingress* is caused by the circumferential distribution of pressure created by the blades and vanes in the turbine annulus: ingress occurs in those regions where the external pressure is higher than that in the wheel-space, and egress occurs where it is lower. Although EI ingress is the dominant mechanism for hot-gas ingestion in engines, there are some conditions in which RI ingress has an influence: this is referred to as *combined ingress (CI)*.

In Part 1 of this two-part paper, values of the sealing effectiveness (obtained using the incompressible orifice equations developed for EI ingress in an earlier paper) are compared with published experimental data and with results obtained using 3D steady compressible CFD (Computational Fluid Dynamics). Acceptable limits of the incompressible-flow assumption are quantified for the orifice model; for the CFD, even though the Mach number in the annulus reaches approximately 0.65, it is shown that the incompressible orifice equations are still valid. The results confirm that EI ingress is caused predominantly by the *magnitude* of the peak-to-trough circumferential difference of pressure in the annulus; the *shape* of the pressure distribution is of secondary importance for the prediction of ingress. A simple equation, derived from the orifice model, provides a very good correlation of the computed values of effectiveness. Using this correlation, it is possible to estimate the minimum sealing flow rate to prevent ingress without the need to know anything about the pressure distribution in the annulus; this makes the orifice model a powerful tool for rim-seal design.

NOMENCLATURE

A, A'	constants in equation for variable $C_{d,e}$
b	radius of seal
c	concentration; speed of sound ($=\sqrt{\gamma RT}$)
$C_{d,e}, C_{d,i}$	discharge coefficients for egress, ingress
C_p	pressure coefficient ($=(p_2-p_1)/\frac{1}{2}\rho\Omega^2 b^2$))
$C_{p,max}$	pressure coefficient ($=\Delta p/\frac{1}{2}\rho W^2$)
C_w	nondimensional flow rate ($=\dot{m}/\mu b$)
$C_{w,e}, C_{w,i}$	nondimensional flow rate for egress, ingress
$C_{w,min}$	minimum value of $C_{w,0}$ to prevent ingress
$C_{w,0}$	nondimensional sealing flow rate
C_{β_1}	modified internal swirl ratio ($=\beta_1^2/(1-r_1^2/r_2^2)$)
C_{β_2}	modified external swirl ratio ($=\beta_2^2/(r_2^2/r_1^2-1)$)
f	shape factor for annulus pressure (see eq (A9))
g	normalized wheel-space pressure (see eq (A10))
$g*$	value of g when $C_{w,0}=0$
G	wheel-space gap ratio ($=s/b$)
G_c	seal-clearance ratio ($=s_c/b$)
I	integrals for EI model (see eqs (A13)-A(15))
K	parameter for EI asymptote
M	Mach number ($=V/c$)
$\dot{m}$	mass flow rate
N	number of vanes
p	absolute static pressure

P_{max}	nondimensional pressure parameter ($=\frac{1}{2}C_{p,max}\,Re_w{}^2$)
r	radius
r_{inner}	inner radius of annulus
r_{outer}	outer radius of annulus
R	gas constant
Re_W	axial Reynolds number in annulus ($=\rho Wb/\mu$)
Re_ϕ	rotational Reynolds number ($=\rho\Omega b^2/\mu$)
s	axial clearance between rotor and stator in wheel-space
s_c	seal clearance
T	absolute temperature
V	velocity through seal clearance
V_r, V_ϕ	radial, tangential components of velocity
W	axial velocity in annulus
x	nondimensional axial distance ($=2z/s_c$)
y	nondimensional radial distance ($=(r-r_{inner})/(r_{outer}-r_{inner})$)
$y+$	nondimensional distance from wall ($=\sqrt{\tau_W/\rho}$)
z	axial distance from centre of seal clearance
β	swirl ratio ($=V_\phi/\Omega r$)
$\delta A_e, \delta A_i$	elemental areas in orifice ring
ΔC_p	external pressure coefficient ($=\Delta p/\frac{1}{2}\rho\Omega^2 b^2$)
Δp	peak-to-trough pressure difference in annulus ($=p_{2,max}-p_{2,min}$)
Γ_C	ratio of discharge coefficients ($=C_{d,i}/C_{d,e}$)
Γ_p	pressure parameter ($=C_p/C_{\beta_1}$)
Γ_β	swirl parameter ($=C_{\beta_2}/C_{\beta_1}\approx(\beta_2/\beta_1)^2$)
ε	sealing effectiveness ($=C_{w,o}/C_{w,e}=\Phi_o/\Phi_e$)
ε_c	computed effectiveness ($=(c_s-c_a)/(c_o-c_a)$)
Φ	nondimensional sealing parameter ($=C_w/2\pi G_c\,Re_\phi$)
Φ_i	value of Φ when $C_w=C_{w,i}$
Φ_i*	value of Φ_i when $\Phi_o=0$
Φ_{min}	value of Φ when $C_w=C_{w,min}$
Φ_o	value of Φ when $C_w=C_{w,0}$
ϕ	angular coordinate in annulus
γ	ratio of specific heats
η_t	modified turbulent flow parameter ($=\lambda_T/4\pi$)
λ_T	turbulent flow parameter ($=C_w\,Re_\phi^{-0.8}$)
μ	dynamic viscosity
θ	angular coordinate between vanes
θ'	value of θ where velocity is zero
ρ	density
τ_W	wall shear stress
Ω	angular speed of rotating disc

Subscripts

a	value in annulus
CI	combined ingress
e	egress
EI	externally-induced ingress
i	ingress
max	maximum
min	minimum
o	superposed flow; total value for compressible flow
RI	rotationally-induced ingress
s	value on stator
1,2	locations in wheel-space and annulus (see Fig. 4)
*	value when $C_{w,0}=0$

1. INTRODUCTION

Fig. 1a illustrates a typical high-pressure gas-turbine stage where cooling of the turbine components allows the mainstream gas temperature to exceed the material's melting point without affecting the blade and vane integrity. Fig. 1b is a simplified view of the stage showing the rim seal and the wheel-space between the stator and the rotating turbine disc. It is important to prevent the ingestion of hot mainstream gas into the wheel-space; this is achieved by supplying the required quantity of cooling and sealing air, which flows outwards over the disc faces. The flow is usually controlled by an inner seal (not shown in Figs. 1a/b) and is expelled from the wheel-space into the mainstream through the rim seal.

The flow past the stationary vanes and rotating blades in the turbine annulus creates an unsteady 3D variation of pressure radially outward of the rim seal. Ingress and egress occur through those parts of the seal clearance where the external pressure is higher and lower, respectively, than that in the wheel-space; this non-axisymmetric type of ingestion is referred to here as *externally-induced* (EI) ingress. Although the sealing air can reduce ingress, too much air reduces the engine efficiency and too little can cause serious overheating, resulting in damage to the turbine rim and blade roots.

Rotating fluid in the wheel-space creates a radial gradient of pressure, so that the pressure inside the wheel-space can drop below that outside. So, even when there is no circumferential variation of external pressure, ingress can still occur. The so-called 'disc-pumping effect' causes a radial outflow of fluid, or egress, near the rotating disc, and the low pressure in the wheel-space causes ingress of external fluid through the rim seal into the wheel-space. This type of ingestion is referred to here as *rotationally-induced* (RI) ingress.

In gas turbines, EI ingress is usually the dominant type of ingestion. However, in double rim seals (like that shown in Fig. 1) the circumferential variation in pressure is attenuated in the annular space between the two seals. If this annular space is large enough to damp out the pressure asymmetry, EI ingress dominates for the outer seal and RI ingress for the inner one. The term *combined ingress* is used here for the case where the EI ingress is the same order-of-magnitude as the RI ingress.

Fig. 2 shows a simplified diagram of ingress and egress in the typical rotating-disc rigs that are used to study the ingress problem. Owen [1, 2] derived the orifice equations for incompressible swirling flow and found analytical solutions for the sealing effectiveness.

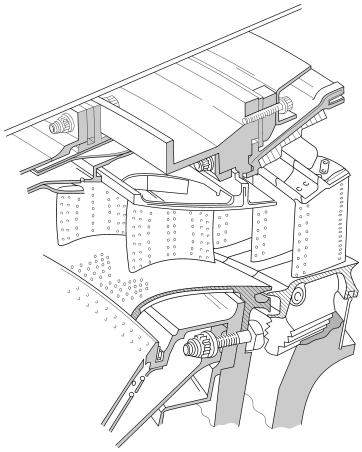

(a) High-pressure turbine stage

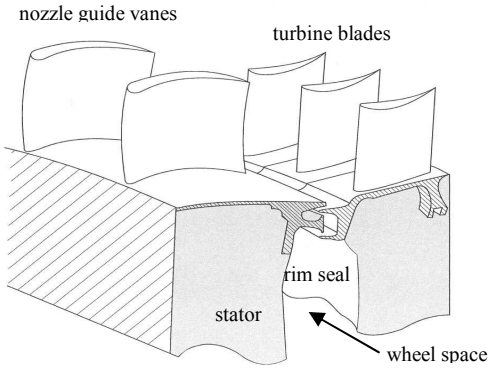

(b) Schematic of rim sea and wheel-space

Fig. 1 Typical rim-sealing arrangement used in gas turbines

It is the principal object of this two-part paper to use CFD (Computational Fluid Dynamics) and previously published experimental data to validate the orifice model for CI and EI ingress. As discussed here, the model not only gives insight into the fluid dynamics of the ingestion processes but it also enables measurements of sealing effectiveness obtained from an experimental rig to be extrapolated to an engine sealing system.

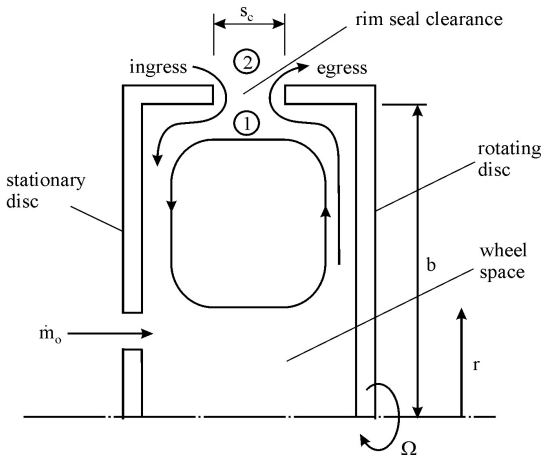

Fig. 2 Simplified diagram of ingress and egress through an axial-clearance rim seal

A brief review of ingress and a summary of the incompressible orifice model are given in Section 2, and solutions of the model are compared with experimental data for the EI case in Section 3. The CFD model is described in Section 4, and solutions of the orifice model are compared with the CFD results in Section 5. The principal conclusions are summarised in Section 6. Appendix A includes a summary of the orifice equations that are referred to in this paper, Appendix B describes how the pressure difference in the annulus is calculated and Appendix C quantifies the range of validity of the incompressibility assumption used in the orifice model.

A large number of parameters and equations are used in this paper but, to make the main body of the text more 'reader friendly,' much of the detailed analysis in placed in the appendices. Despite the complexity of the analysis, the most important equation, eq (5.6), is relatively simple and it is easy to apply. Part 2 of this paper [3] describes the development and validation of the orifice model for the CI case.

2. REVIEW OF INGRESS PROBLEM

As both RI and EI ingress were reviewed in [1, 2], the discussion below includes only those references that are of particular relevance to this paper. The definitions of variables not defined below can be found in the Nomenclature.

2.1 Rotationally-induced ingress

Bayley and Owen [4] presented experimental results for a simple rotor-stator system with an axial-clearance rim seal in

which there was a superposed radial flow of air that discharged through the seal into the atmosphere; there was no external annulus on the rig. Owing to the sub-atmospheric pressure created by the rotating flow in the system, external (atmospheric) air could be drawn into the wheel-space. Increasing the superposed flow rate increased the relative pressure inside the wheel-space and consequently reduced the amount of ingested air. At sufficiently high superposed flow rates, where $C_{w,0} \geq C_{w,min}$, ingress did not occur. (These terms, and those used below, are defined in the Nomenclature, but it should be noted that $C_{w,0}$ is the nondimensional superposed flow rate and $C_{w,min}$ is the minimum value needed to prevent ingress.) Bayley and Owen used their measured pressures for G_c = 0.0033 and 0.0067, and for $Re_\phi \leq 4\times10^6$, to provide the correlation:

$$C_{w,min} = 0.61 G_c Re_\phi \qquad (2.1)$$

Graber *et al.* [5] reported extensive concentration measurements in a rotating-disc rig, which was used to determine the effects of seal geometry, rotational Reynolds numbers and the level of swirl in the external annulus on ε, the sealing effectiveness. Their measurements, which showed that the external swirl had no systematic effect on the effectiveness, were used in [1] to validate the orifice model for RI ingress.

2.2 Externally-induced ingress

Phadke and Owen [6-8] determined $C_{w,min}$ in a simple rotor-stator system with a number of different rim-seal geometries, with and without an external flow of air. There were no vanes or blades in the external annulus of their rig, and circumferential pressure asymmetries were obtained by blocking sections of the annulus with wire mesh. The authors observed both RI ingress (where, with no external flow, $C_{w,min}$ increased with increasing Re_ϕ) and EI ingress (where, with non-axisymmetric external flow, $C_{w,min}$ was independent of Re_ϕ and increased with increasing Re_w, the axial-flow Reynolds number in the external annulus).

Phadke and Owen [8] correlated their results for EI ingress, based on flow visualization, for a number of different seal geometries, by:

$$C_{w,min} = 2\pi K G_c P_{max}^{\frac{1}{2}} \qquad (2.2)$$

where

$$P_{max} = \frac{1}{2} C_{p,max} Re_w^2 \qquad (2.3)$$

$C_{p,max}$ is a nondimensional pressure difference in the external annulus and K is an empirical constant; the data were correlated with K = 0.6.

Hamabe and Ishida [9] made measurements of the sealing effectiveness in a turbine rig fitted with upstream guide vanes but with no downstream blades. For EI ingress, they correlated the effectiveness of a simple axial-clearance seal with a nondimensional parameter similar to that used by Phadke and Owen, and the results of their orifice model were in reasonable agreement with their measurements. They also showed that, as discussed in Part 2, the discharge coefficient for egress, $C_{d,e}$, decreased as the external flow rate increased.

Chew *et al.* [10] made effectiveness measurements in a rig with upstream nozzles in the annulus; their orifice model performed less well than that of Hamabe and Ishida in predicting the effectiveness but their steady 3D CFD computations gave encouraging results. They also measured the discharge coefficients for the rim seal when there was no disc rotation. The measurements, like those of Hamabe and Ishida, showed that $C_{d,e}$ decreased monotonically with increasing external flow rate.

Bohn and Wolff [11] presented a correlation for the sealing effectiveness, ε, in terms of $C_{w,0}$, G_c and $C_{p,max}$, and their correlations for the four seal geometries shown in Fig. 3 display the linear variation of $C_{w,min}$ with $C_{p,max}^{1/2}$ that was found by Phadke and Owen; the value of K = 0.6 suggested by the latter authors produces a conservative estimate for $C_{w,min}$.

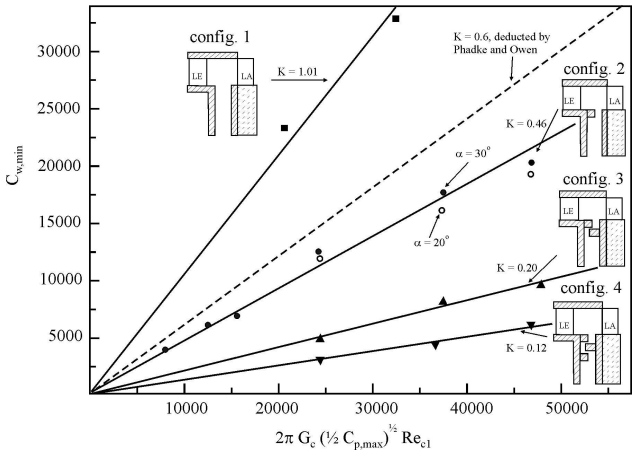

Fig. 3 Variation of $C_{w,min}$ with $C_{p,max}$ [11]

(Symbols represent experimental data; lines correspond to correlations.)

Johnson *et al.* [12] used an orifice model to obtain good predictions of the effectiveness measurements in the turbine rig of Bohn *et al.* [13]. They used the values obtained from 2D time-dependent CFD to determine the external circumferential pressure distribution in their model, which allowed the effects of the vane wakes and the blade bow waves to be taken into account. A modified version of their orifice model was also successfully applied by Johnson *et al.* [14] to the ingress measurements made on a turbine rig in Arizona State

University. Owen [2], using the orifice model described below, obtained good agreement between the predicted effectiveness and the measured values presented in [12] and [14].

2.3 Orifice model for incompressible swirling flow

Appendix A summarises the incompressible orifice equations for RI and EI ingress.

The mathematical model for the orifice equations derived in [1] is based on an *orifice ring*, as shown in Fig. 4 for an axial-clearance seal, where ingress and egress simultaneously cross different parts of an imaginary ring. (The orifice ring can be thought of as a thin circular membrane with the same dimensions as the seal clearance.) Egress flows through a stream tube in the wheel-space where the static pressure is p_1 and, after crossing the ring through a small orifice with an area δA_e, emerges in the external annulus where the static pressure is p_2; conversely, ingress originates in the annulus and, after crossing the ring through an orifice with an area δA_i, emerges in the wheel-space.

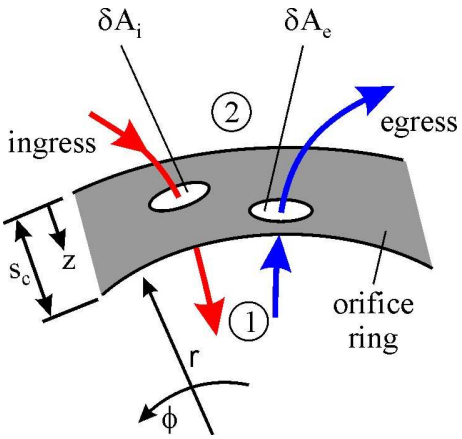

Fig. 4 Schematic of orifice model [1]

It is assumed that there is continuity of mass and energy inside the separate stream tubes for egress and ingress but there is a discontinuity in the pressure across the sealing ring. In addition, angular momentum is conserved, so that free-vortex flow occurs and rV_ϕ is constant. The principal 'orifice assumptions' are that $(r_2 - r_1)/r_1 << 1$, and that $V_{r,1}^2 << V_{r,2}^2$ for egress and *vice versa* for ingress. Although the equations are derived for inviscid incompressible flow, discharge coefficients, analogous to those used for the standard orifice equations, are introduced to account for losses. In general, different discharge coefficients ($C_{d,i}$ and $C_{d,e}$) are needed for ingress and egress, and these have to be determined empirically.

For rotationally-induced (RI) ingress, the flow is assumed to be axisymmetric: swirl of the flow in the wheel-space is included but external pressure asymmetries are ignored. For the RI special case (where $C_{d,i} = C_{d,e}$ and external flow is negligible), the solutions of the equations, used in conjunction with the Bayley-Owen correlation for $C_{w,min}$ given in eq (2.1), were in mainly good agreement with the effectiveness measurements of Graber *et al.*

For EI ingress, the circumferential variation of pressure in the annulus is included but swirl in the wheel-space is ignored. In a turbine with N nozzle guide vanes, it is convenient to define

$$\theta = \frac{N}{2\pi}\phi \qquad (2.4)$$

so that, for $0 \le \phi \le 2\pi/N$, $0 \le \theta \le 1$ and $p_2 = p_2(\theta)$ is the time-average external pressure between each pair of vanes. For simplicity, it is assumed that p_1, the pressure at some suitable location in the wheel-space, is axisymmetric. Although the locations for the measurement of p_1 and p_2 do not feature explicitly in the solutions of the orifice equations, they will, as shown in Section 5, affect the value of the discharge coefficients derived from experimental measurements. To obtain analytical solutions for EI ingress, the circumferential variation of pressure in the annulus was approximated in [2] by a saw-tooth model (see Fig. A1 in Appendix A).

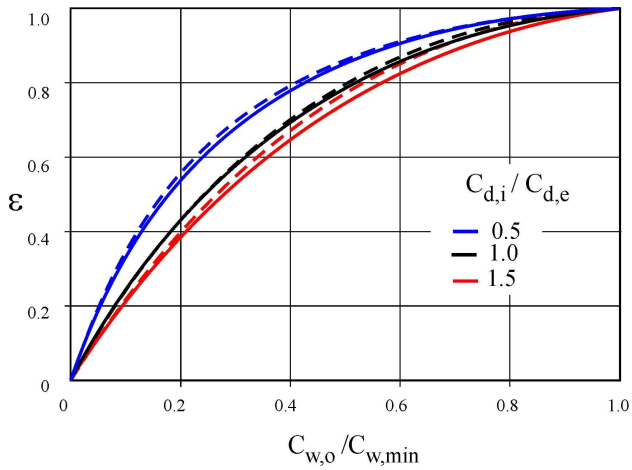

Fig. 5 Effect of $C_{d,i}/C_{d,e}$ on variation of ε with $C_{w,o}$ predicted by orifice model [2].
Solid line, EI ingress; dashed line, RI ingress.

Fig. 5 shows the variation of the effectiveness with sealing flow rate predicted by the orifice model for RI and EI ingress. It can be seen that, as expected, the effectiveness increases as

the ratio of $C_{d,i}/C_{d,e}$ decreases. It can also be seen that, despite the difference between the EI and RI equations, the two sets of solutions are very similar. The solutions show that, for the special case where $C_{d,i}=C_{d,e}$, the maximum possible ingestion for both EI and RI ingress is around 35% of the flow rate needed to prevent ingress.

3. COMPARISON BETWEEN ORIFICE MODEL AND EXPERIMENTAL DATA

In [2], the saw-tooth model for EI ingress was compared with the data of Johnson *et al.* [12], which were based on measurements made by Bohn *et al.* [13]. In the experimental rig, in which the blades and vanes had a variable axial separation, the seal-clearance ratio was $G_c = 0.0296$.

In this paper, the full orifice equations are solved using the pressure distributions given by Johnson *et al.* for their configurations Conf 1a and 1c. Figs 6a and 6b show the distribution of the nondimensional pressure or shape factor f for Conf 1a and 1c respectively. The definition of the shape factor, which is defined in eq (A9), is repeated below for convenience:

$$f(\theta)=\frac{p_2-p_{2,min}}{\Delta p} \qquad (3.1)$$

for the range $0\le f(\theta)\le 1$, where $0\le\theta\le 1$ is the relative angular position (between the vanes in a rig or an engine), and $\Delta p = p_{2,max}-p_{2,min}$ is the peak-to-trough pressure difference in the annulus.

Conf 1a (where the measurements were made for the wheel-space *upstream* of the blades) corresponded to close spacing between the vanes and blades, where $\Delta C_p \approx 0.55$; Conf 1c (for the *downstream* wheel-space) was for a wider spacing, with $\Delta C_p \approx 0.085$. (It should be noted that ΔC_p, which is defined in the Nomenclature, is the nondimensional peak-to-trough pressure difference in the external annulus; it is the main driving force for EI ingress.)

In their orifice model, Johnson *et al.* used a time-average fit of the circumferential distribution of pressure (computed by CFD at the upstream edge of the seal clearance at a radial distance of 10% of the blade height). Their computed distribution was approximated here to provide the 'fitted' distribution of f shown in Fig. 6. The saw-tooth distribution and a cosine approximation of f are also shown in this figure. *It should be noted that the cosine approximation, unlike the saw tooth, allows no simple analytical solutions of the orifice equations.*

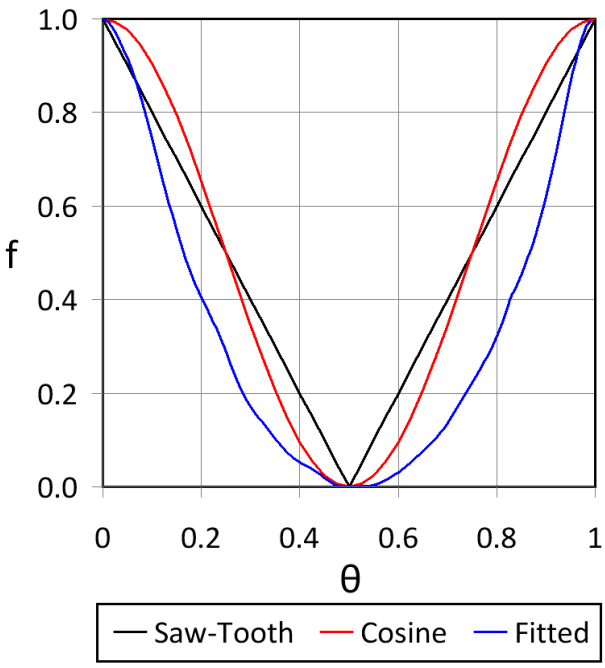

(a) Conf 1a

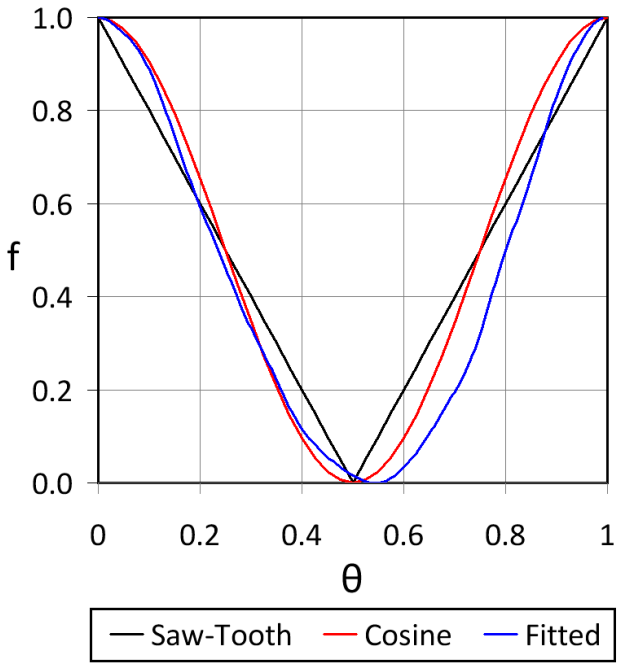

(b) Conf 1c

Fig. 6 Variation of f, the pressure shape-factor, with θ, the angular location in the annulus, based on data of Johnson *et al.* [12]

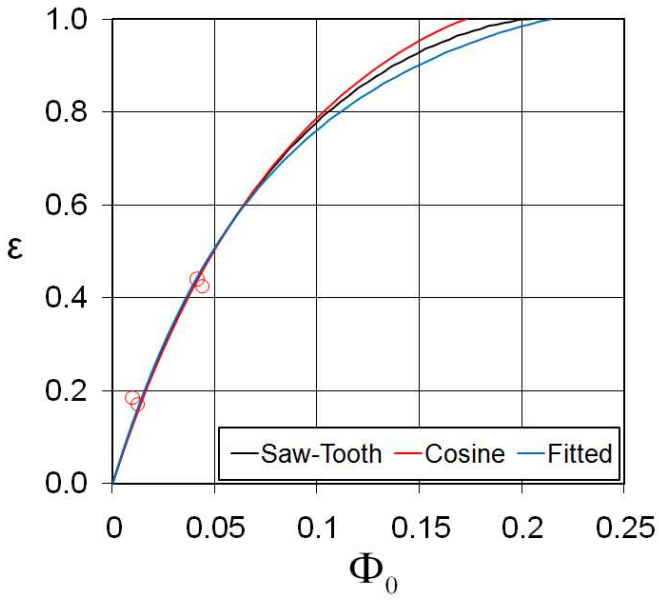

(a) Conf 1a

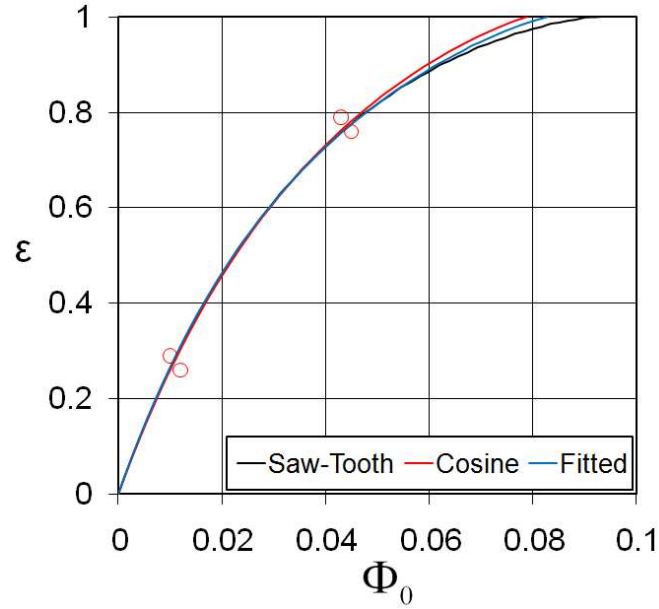

(b) Conf 1c

Fig. 7 Variation of ε, the sealing effectiveness, with Φ_o, where $\Phi_o = C_{w,o} / 2\pi G_c\ Re_\phi$.
(Symbols represent corners of envelope of experimental data given by Johnson *et al.* [12].)

The three *f*-distributions were integrated numerically to obtain the integrals I_e, I_i and I_{min}, defined by eqs (A13-A15), and ε, the sealing effectiveness, was then calculated using eq (A12) with $\Gamma_c = 1$ (where $\Gamma_c = C_{d,e} / C_{d,i}$). The computed variations of ε with Φ_o (where $\Phi_o = C_{w,o} / 2\pi G_c\ Re_\phi$) are shown in Figs 7a and 7b for Confs 1a and 1c respectively. (It should be noted that Φ_o is mathematically equivalent to the ratio of the radial velocity of the sealing air through the seal clearance to the rotational speed of the disc; this ratio was used by Johnson *et al.* to correlate their data.)

Rather than showing the discrete data points in their paper, Johnson *et al.* bounded their experimental values of ε with a rectangular envelope, and the symbols shown in the figures represent the corners of that envelope. The computed effectiveness curves were arbitrarily matched to the centroid of the data envelope: this is equivalent to choosing a value of $\Phi_{min,EI}$ that gives the 'best fit' to a *single* data point. (With access to all the experimental data, it would have been possible to use the method described in Section 5 below to find the optimum values of both Γ_c and $\Phi_{min,EI}$.)

From Appendix A, eq (A11) shows that

$$\Phi_{min,EI} = \frac{C_{w,min,EI}}{2\pi G_c\ Re_\phi} = I_{min} C_{d,e,EI}\ \Delta C_p^{\,1/2} \qquad (3.2)$$

where the integral I_{min} is defined by eq (A13); for the saw-tooth model, I_{min} = 2/3. After evaluating $\Phi_{min,EI}$ and I_{min}, $C_{d,e,EI}$ can be calculated from eq (3.2), and the calculated values are given in Tables 1a and 1b for Confs 1a and 1c, with the respective values of ΔC_p taken to be 0.55 and 0.085.

f-distribution	$\Phi_{min,EI}$	I_{min}	$C_{d,e}$	K
Fitted	0.215	0.756	0.377	0.403
Cosine	0.173	0.637	0.360	0.324
Saw-Tooth	0.205	0.667	0.408	0.384

(a) Conf 1a ($\Delta C_p \approx 0.55$)

f-distribution	$\Phi_{min,EI}$	I_{min}	$C_{d,e}$	K
Fitted	0.083	0.674	0.422	0.403
Cosine	0.079	0.637	0.425	0.383
Saw-Tooth	0.093	0.667	0.479	0.451

(b) Conf 1c ($\Delta C_p \approx 0.085$)

Table 1 Computed parameters for data of Johnson *et al.* [12]

Assuming that the fitted distribution gives the most accurate of the three estimates of the orifice parameters, it can be seen that the saw-tooth value of $\Phi_{min,EI}$ is more accurate than the cosine value for Conf 1a but is less accurate for Conf 1c. For both configurations, the fitted distribution and the cosine approximation give values of $C_{d,e,EI}$ that agree with the value of 0.4 given by Johnson *et al.* (who rounded $C_{d,e,EI}$ to one-significant-figure accuracy). The saw-tooth model gives a value of $C_{d,e,EI}$ consistent with that of Johnson *et al.* for Conf 1a but it overestimates the 0.4 value for Conf 1c.

It can be seen from Table 1 that the value of $\Phi_{min,EI}$ is more affected by the *magnitude* of ΔC_p than by the *shape* of the circumferential distribution of pressure. It should also be noted that the values computed by Johnson *et al*. were based on *all* the available experimental data rather than the data envelope used here. In addition, the values of $\Phi_{min,EI}$ shown in Table 1b for Conf 1c are smaller than the value of $\Phi_{min,RI}$ = 0.097 obtained from the Bayley-Owen correlation given in eq (2.1) for RI ingress; as discussed in Part 2, this suggests that the experimental conditions for Conf 1c were more consistent with CI ingress than with EI ingress.

K, which is defined in eq (2.2), is a parameter commonly used for ranking the relative performance of different seal geometries. Using the definitions in the Nomenclature, it can be shown that

$$K = \sqrt{2}\, C_{d,e,EI}\, I_{min} = \sqrt{\frac{2}{\Delta C_p}}\, \Phi_{min,EI} \qquad (3.3)$$

and values of K are included in Table 1. Bohn and Wolff [11] correlated their experimental data for an axial-clearance seal with K = 0.46. In the light of the observations made in Section 5 below, it is surprising and perhaps fortuitous that this value is as close as it is to those obtained using the orifice model.

The following conclusions can be drawn from the above results. The peak-to-trough pressure difference in the annulus is the principal driving force for EI ingress; the *shape* of the pressure distribution is of secondary importance. The cosine approximation to the pressure distribution has the disadvantage that it requires numerical integration of the orifice equations, and it is not significantly more accurate than the analytical saw-tooth model in calculating $\Phi_{min,EI}$ and K.

As shown in Section 5, the great advantage of the saw-tooth model is that it allows analytical solutions of the sealing effectiveness to be determined without the need to know either the peak-to-trough pressure difference or the shape of the pressure distribution in the annulus.

4. COMPUTATIONAL MODEL

Computational results in the present work were obtained using a 3D steady flow computational model. Other recent computational studies of ingestion, and of the performance of different turbine rim seals, have been reported by, for example, Laskowski *et al.* [15], Rabs *et al.* [16], Zhou *et al.* [17] and Mirzamoghadam *et al.* [18, 19]. Laskowski *et al.* noted that Hills *et al.* [20] studied ingress computationally using both steady and unsteady three-dimensional models, finding that models with fixed locations of a rotor peg (as used in an experimental rig to represent turbine blades) relative to the vane trailing edge gave rise to very low levels of predicted ingress into the wheel-space. This is the so-called "frozen-rotor" approach. Only unsteady computations, with the peg rotating relative to the vane (using a sliding plane at the interface of the rotating and stationary sections of the computational model) predicted levels of ingress that accorded with values of effectiveness ε measured in experiments.

Laskowski *et al.* found that only with an unsteady model did ingress penetrate the outer 'angel-wing' seal of their buffer cavity configuration. Mirzamoghadam *et al.* [19] carried out both steady and unsteady computations for a 'double-overlap' rim seal geometry (with the stator overlapping the rotor), and studied the effects of annulus flow Reynolds number (hence the magnitude of the pressure asymmetry due to the stator vane). Like others, Mirzamoghadam *et al.* concluded that the vane wake dominates over the blade bow wave in determining ingestion mechanisms. The use of a steady model in the present work is discussed further below.

The commercial CFD code CFX-11 was used for the computations presented in this paper. The model geometry, illustrated in Figs 8 and 9, was based on the generic vanes that will be used in an experimental rig currently being built at Bath. The model comprises one vane pitch of a ring of 32 stationary vanes in an external annulus, the radial height of which is 10 mm. (As one of the experimental objectives is to compare the performance of different seal geometries, the 'lossy' generic vane profile illustrated in Fig. 9 was chosen to produce a large value of ΔC_p in the annulus.) Cyclic symmetry conditions are applied at the circumferential faces of the 11.25º sector model.

The gap ratio for the wheel-space is G = 0.1 and the axial seal-clearance ratio studied here is G_c = 0.01. The wheel-space is bounded by a rotor-side axial-clearance inner seal at r/b = 0.86, with a superposed sealing flow rate prescribed at this clearance as shown in Fig. 8. A linear variation of swirl was applied so that the sealing flow enters with zero swirl at the stationary edge of the inlet and at the speed of the disc at the rotor surface.

The flow rates and rotational speed considered correspond to $Re_w = 8.5 \times 10^5$, $0 < C_{w,o} < 1.7 \times 10^4$ and $Re_\phi = 1.03 \times 10^6$, based on the inner radius b = 195 mm of the seal; the isentropic Mach number in the annulus is approximately 0.65. The fluid properties for all the nondimensional parameters are

based on conditions at outlet from the annulus (p = 1.01 bar, T = 298K).

The object of the computations was to provide a realistic circumferential pressure distribution in the annulus in order to drive ingress across the seal clearance. Mesh sensitivity studies were carried out as a result of which a model having approximately 1.7 million cells was used; this mesh is illustrated in Fig. 9. The hexahedral mesh (produced using the ICEM software) was refined near wall surfaces so that the SST model of turbulence could be used with y+ < 2 on the surfaces of the rotor and stator in the wheel-space; y+ > 10 was observed for the surfaces of the stationary vane.

A discretised passive-scalar concentration equation was solved, in addition to the Navier-Stokes equations for mass and momentum, so that the effectiveness based on this computed concentration could be calculated. The scalar was introduced with a concentration of unity along with the prescribed wheel-space sealing flow, while a zero value was applied at the annulus mainstream flow inlet. An ambient (atmospheric) average-pressure condition was applied at the annulus outlet boundary. The perfect gas law was used to compute the fluid density, with thermal effects neglected. (Windage will affect the fluid temperature and hence the density, but this effect was considered to be small at the rotational speeds considered here.) The no-slip condition was applied at solid surfaces.

Typical convergence levels were less than 10^{-6} for the normalized rms residuals, and total elapsed computing times of around 10 hours (using a single 2.8GHz processor) were required for each case computed.

Simplifications, such as prescribed periodicity and steady flow, can cause the under-prediction of ingress. This is due in part to the computed formation of substantial recirculation in the seal-clearance region, see for example Lewis and Wilson [21]. In the computations reported here, a 'thin seal' approximation is employed, in which the radial dimension of the seal is made as thin as permitted by meshing considerations in the seal-clearance region, see Fig. 9. The use of this modified seal geometry inhibits the formation of a vortex inside the seal-clearance. (Computations were originally carried out using an infinitesimally-thin 'baffle-type' condition at solution cell faces at the seal radius. This created difficulties with post-processing to obtain the ingress and egress flow rates across the seal clearance.)

The results presented below were obtained using the steady model with the thin-seal approximation. To investigate the validity of these simplifications, an extension of the model to unsteady flow (incorporating rotating blades and the actual seal geometry) has also been tested. The results of these unsteady computations are described by Zhou *et al.* [22]. The values of effectiveness computed were similar to, but slightly lower than, those computed using the steady model.

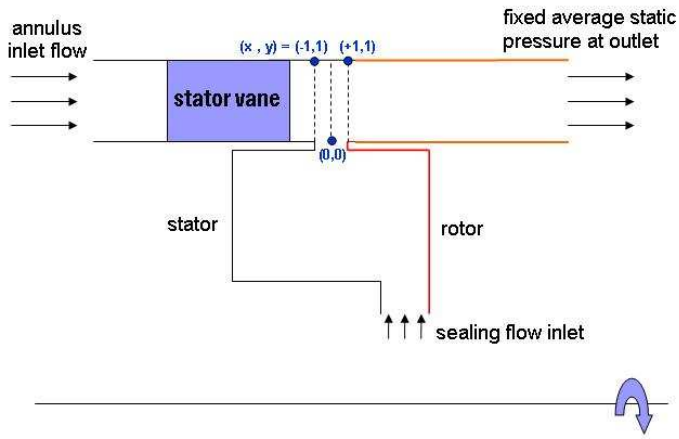

Fig. 8 Illustration of computational geometry (not to scale)

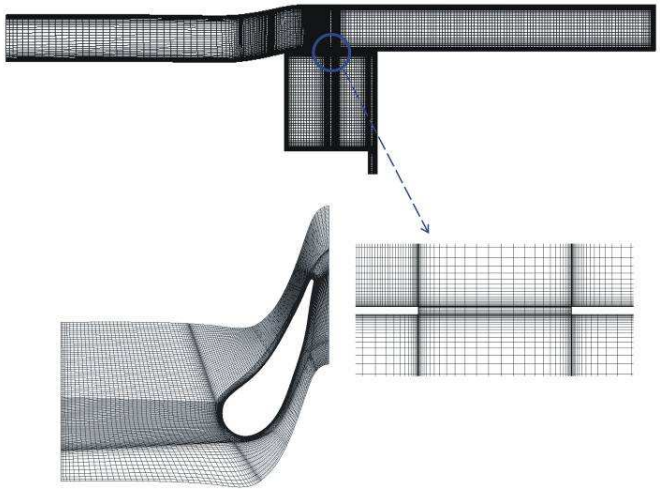

Fig. 9 Computational mesh with detail of generic vane profile and clearance region for 'thin-seal' model.

5. COMPARISON BETWEEN SAW-TOOTH MODEL AND CFD SOLUTIONS

All computations were conducted for Re_ϕ = 1.03 x 10^6 and $G_c = 0.01$. The definitions of symbols used below are given in the Nomenclature, and the relevant results of the saw-tooth model are summarised in Appendix A4.

Not only do the CFD solutions throw light on the flow structure and create data for the orifice model, they also provide criteria for the choice of the locations of stations 1 and 2 (see Fig. 4) that feature in the orifice equations.

5.1 Computed flow structure in wheel-space

As the object of this section of the paper is to show comparisons between the computed effectiveness and the theoretical effectiveness produced from the orifice model, only

those aspects of the flow structure relative to this object are discussed here. More details of the computed flow structure for steady and unsteady flow are given by Zhou *et al.* [22].

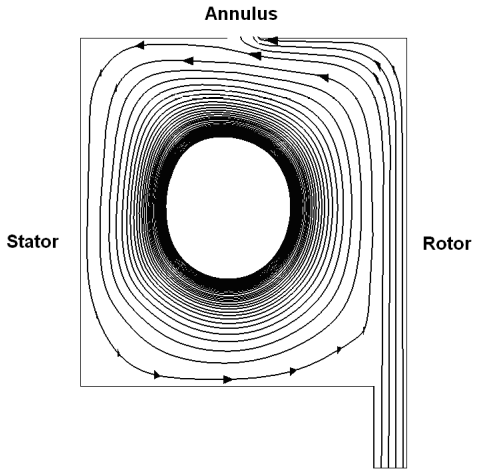

(a) Flow structure

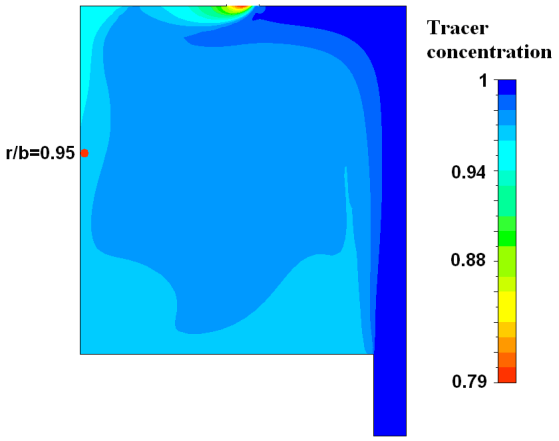

(b) Concentration contours

Fig. 10 Computed flow structure and concentration inside wheel-space: $Re_\phi/10^6 = 1.03, C_{w,o}/10^4 = 1.69$

Fig. 10 shows the computed flow structure and concentration contours at one circumferential $r-z$ plane inside the wheel-space for Re_ϕ = 1.03 x 10^6 and $\Phi_o = C_{w,o}/2\pi G_c\, Re_\phi$ = 0.259, where Φ_o is the nondimensional sealing flow rate. Fig. 10a shows the familiar rotor-stator flow structure with radial outflow on the rotating disc and inflow on the stator. In addition to the primary superposed sealing flow, there is an anti-clockwise secondary circulation in which fluid flows from the stator to the rotor at the smaller radii and from the rotor to the stator at the larger radii.

The concentration contours in Fig. 10b are equivalent to the local effectiveness where unity (indicated by the blue colour) is the concentration of the sealing flow and zero is that of the annulus. For this relatively large flow rate, where there is only a small amount of ingress, most of the ingested fluid is confined to a small mixing region between the ingress and the egress flows near the seal clearance. The maximum concentration in this mixing region (indicated by red) is approximately 0.79. There is also an external mixing region in the annulus (not shown here) where the ingress and egress flows mix outside the wheel-space. Consequently the concentration of the ingested fluid always exceeds that in the annulus. After leaving the mixing region, the ingested fluid enters the boundary layer on the stator before being entrained into the boundary layer on the rotor, where the sealing air buffers the rotating disc from the ingested fluid.

At lower sealing flow rates, which are not shown here, ingress increases, the mixing region becomes larger and the ingested fluid can enter the boundary layer on the rotating disc as well as that on the stator. The exchange of angular momentum between the sealing flow and the ingested fluid increases the swirl inside the wheel-space; if the local swirl ratio exceeds unity (i.e. $V_\phi/\Omega r > 1$ in the core between the boundary layers), radial *inflow* occurs in the boundary layer on the rotor as well as in that on the stator. Under these conditions, the ingested fluid can make direct contact with the rotating disc; this could have serious consequences in an engine. This is discussed further in [22].

At the smaller radii, fluid leaves the boundary layer on the stator to be entrained by the boundary layer on the rotating disc. As, outside the mixing region, no fluid is entrained *into* the stator boundary layer, it follows that the value of the effectiveness on the stator wall does not vary significantly with the radial location. For convenience, the location of station 1 for the orifice equations (see Fig. 4) was arbitrarily taken to be r/b = 0.95 on the surface of the stator, and the computed effectiveness values discussed below were based on this location.

5.2 Determination of effectiveness

The computations were conducted for the geometry described in Section 4 with G_c = 0.01 and Re_ϕ = 1.03 x 10^6.

The computed effectiveness, ε_c, is defined as

$$\varepsilon_c = \frac{c_s - c_a}{c_o - c_a} \qquad (5.1)$$

where c_s, c_o and c_a are respectively the concentrations on the stator, in the sealing flow at inlet to the wheel-space and in the upstream flow through the annulus. For the reasons discussed above, the value of c_s was the value of the

concentration on the stator surface at r/b = 0.95; the values of c_a and c_o were kept constant so that the effectiveness depended only on the value of c_s. It follows that $\varepsilon_c = 1$ when there is no ingress (such that $\Phi_o = \Phi_{min,EI}$) and $\varepsilon_c = 0$ when the sealing flow rate is zero ($\Phi_o = 0$).

The effectiveness ε used in the orifice model, which is based on the convection of fluid created by pressure differences, can be defined as

$$\varepsilon = \frac{C_{w,o}}{C_{w,e}} \tag{5.2}$$

In the mass-transfer equation, concentration differences in the fluid create diffusion and mixing, which are additional to the convection of fluid predicted by the orifice model. Consequently, the two definitions of effectiveness are similar but are not generally equivalent. Despite this, it is usual to match the computed and theoretical results by implicitly *assuming* that they are equivalent. This is, in effect, like 'calibrating' the orifice model by optimizing the appropriate empirical parameters to fit the effectiveness data, as discussed in Section 5.3.

It is convenient to reproduce eqs (A22) and (A26) in Appendix A4 for the saw-tooth model, where

$$\frac{\Phi_o}{\Phi_{min,EI}} = \frac{C_{w,o}}{C_{w,min,EI}} = g^{3/2} - \Gamma_c (1-g)^{3/2} \tag{5.3}$$

and

$$\varepsilon = 1 - \Gamma_c \left[\frac{1-g}{g}\right]^{3/2} \tag{5.4}$$

where g, the normalised pressure in the wheel-space, is defined as

$$g = \frac{p_1 - p_{2,min}}{\Delta p} \tag{5.5}$$

for the range $g^* \le g \le 1$, where g^* is the value of g when the superposed flow rate is zero ($\Phi_o = 0$). It should be noted that $\Gamma_c = C_{d,i} / C_{d,e}$, the ratio of the discharge coefficients for ingress and egress, and $\Delta p = p_{2,max} - p_{2,min}$, the peak-to-trough pressure difference in the annulus. Consistent with the effectiveness computations referred to above, the location for p_1 in the wheel-space is at r/b = 0.95 on the stator surface.

By eliminating g from eqs (5.3) and (5.4), it can be shown that

$$\frac{\Phi_o}{\Phi_{min,EI}} = \frac{C_{w,o}}{C_{w,min,EI}} = \frac{\varepsilon}{[1 + \Gamma_c^{-2/3}(1-\varepsilon)^{2/3}]^{3/2}} \tag{5.6}$$

Eq (5.6) uncouples cause (the pressure difference, Δp) from effect (the effectiveness, ε) and, as shown below, this equation provides a simple and powerful means of correlating the effectiveness data.

5.3 Determination of $\Phi_{min,EI}$ and Γ_c from effectiveness data

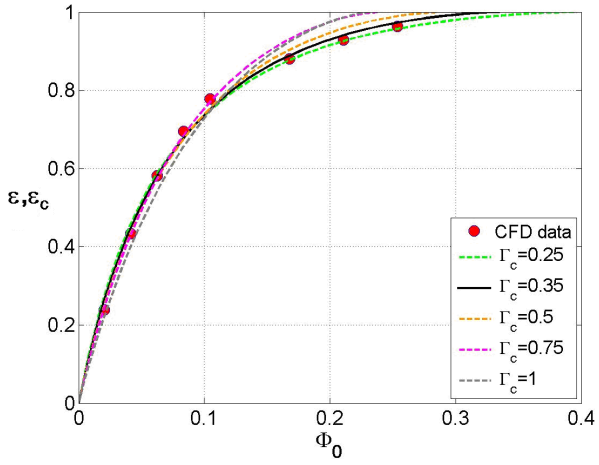

Fig. 11 Comparison between computed and theoretical variation of effectiveness with nondimensional sealing flow rate for $\mathrm{Re}_\phi = 1.03\times10^6$, $G_c = 0.01$. ($\Phi_o = C_{w,o} / 2\pi G_c \mathrm{Re}_\phi$ and $\Gamma_c = C_{d,i} / C_{d,e}$ = 0.35 is the optimum value for the saw-tooth model.)

Fig. 11 shows a comparison between the computed data and the theoretical variation of effectiveness according to eq (5.6) for various values of Γ_c. The fit between this equation and the computed variation of ε_c with Φ_o was optimized using a regression analysis, in which values of Γ_c and $\Phi_{min,EI}$, the 'primary empirical parameters' for the saw-tooth model, were chosen to minimize the least-squares error between the data and the theoretical curves. (As shown in Section 5.5, the determination of Γ_c and $\Phi_{min,EI}$ implicitly determines the values of $C_{d,e}$ and $C_{d,i}$.)

The optimum fit was achieved with Γ_c = 0.35 and $\Phi_{min,EI}$ = 0.335, and it can be seen that the agreement between the optimum theoretical curve and the computed data is very good. It can also be seen that the theoretical value of $\Phi_{min,EI}$ (where ε = 1) increases significantly as Γ_c decreases. (In principle, the values of $\Phi_{min,EI}$ and Γ_c could be estimated from only two data points; the regression analysis used here, for the eight data points, gives a more accurate estimate.)

The maximum nondimensional ingress, $\Phi_i{}^*$, which occurs when Φ_o=0, can be determined from eq (A24):

$$\frac{\Phi_i^*}{\Phi_{min,EI}} = \frac{C_{w,i}^*}{C_{w,min,EI}} = \frac{1}{(1+\Gamma_c^{-2/3})^{3/2}} \qquad (5.7)$$

It should be noted that, as $\Phi_o = 0$, $\Phi_i^* = \Phi_e^*$: the maximum ingress corresponds to the *minimum* egress. For the optimum fit where $\Gamma_c = 0.35$, $\Phi_i^* / \Phi_{min,EI} \approx 0.19$. That is, for this value of Γ_c, the maximum ingestion is approximately 19 % of the flow rate needed to prevent ingress. The values of Φ_i^* for all five values of Γ_c are shown in Table 2.

Significantly, ΔC_p, which is the primary cause of EI ingress, is not required by the saw-tooth model to determine $\Phi_{min,EI}$. ΔC_p was used to derive the orifice equations but the uncoupling of pressure from effectiveness has removed it from eq (5.6). *This allows the prediction of* $\Phi_{min,EI}$ *from computational (or experimental) effectiveness data without the need to evaluate* ΔC_p, $C_{d,e,EI}$ *or any other parameter in the external annulus.* (ΔC_p has, in effect, left its fingerprints on the effectiveness data.)

Traditionally, $C_{w,min}$ was the parameter that was computed or measured experimentally. However, the present work shows that $\Phi_{min,EI}$ is a more useful parameter, and the saw-tooth model provides a simple and effective way to evaluate it. Theoretically, $\Phi_{min,EI}$ is independent of the rotational Reynolds number, Re_ϕ; this means that the value of $\Phi_{min,EI}$ determined in an experimental rig at one value of Re_ϕ should be valid for all values of Re_ϕ. (It is implicitly assumed here that the measurements are all made in the EI ingress domain; this is discussed further in Part 2.) This suggests that, providing the rig geometry is similar to that in an engine, the value of $\Phi_{min,EI}$ created in the engine should be the same as that found from measurements at a different value of Re_ϕ in the rig. This hypothesis has yet to be tested!

To satisfy the traditionalists, even though these parameters are not required by the saw-tooth model, ΔC_p and $C_{d,e,EI}$ can be evaluated by the method described below.

5.4 Determination of ΔC_p

For convenience, ΔC_p is defined below:

$$\Delta C_p = \frac{\Delta p}{1/2 \rho \Omega^2 b^2} \qquad (5.8)$$

where $\Delta p = p_{max} - p_{min}$ is the peak-to-trough pressure difference in the annulus. It should be noted that p_{max} and p_{min} are evaluated at different circumferential locations in the annulus.

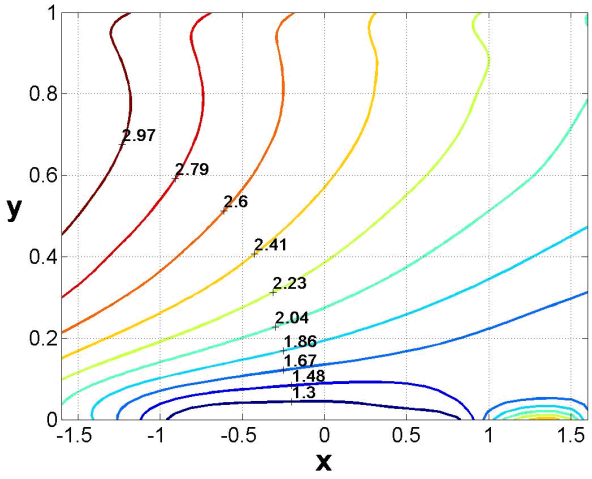

Fig. 12 Contours of ΔC_p computed inside annulus for $\Phi_o = 0$

Fig. 12 shows the computed contours of ΔC_p in the wheel-space for the zero-flow case ($\Phi_o = 0$); this is the case used by most experimentalists. The normalised axial and radial locations, *x* and *y*, used in this figure are defined as

$$x = 2\frac{z}{s_c}, \quad y = \frac{r - r_{inner}}{r_{outer} - r_{inner}} \qquad (5.9)$$

where z is the axial distance from the centre of the seal clearance, s_c is the axial width of the seal, and r_{inner} and r_{outer} are the inner and outer radii respectively of the external annulus. The upstream and downstream edges of the seal clearance are at $x = -1$ and $x = +1$, respectively, and the trailing edge of the vanes is at $x = -6$. The decrease of ΔC_p with x is caused by the decay of the wake from the vanes, and the increase with y is caused by the swirl in the annulus.

It can be seen from Fig. 12 that, between $\Delta C_p = 1.48$ and 1.67, there must be a 'dividing contour' that separates the external flow from the mixing region between ingress and egress near the seal clearance in the annulus. (The dividing contour is analogous to a dividing streamline in the flow of fluid.)

As described in Appendix B, the location for evaluating ΔC_p was chosen using a 'consistency criterion', which satisfies the saw-tooth equations. The location (x,y) = (0.93, 0), near the downstream edge of the seal clearance, was one of the few locations that satisfied this criterion; this location corresponds to station 2 in the orifice equations (see Fig. 4). The computed value of ΔC_p at this location was 1.55, and this value is used below to compute $C_{d,e,EI}$.

5.5 Determination of $C_{d,e,EI}$ and K

It is convenient to rewrite eq (A19) below:

$$\Phi_{min,EI} = \frac{C_{w,min,EI}}{2\pi G_c \, Re_\phi} = \frac{2}{3} C_{d,e,EI} \, \Delta C_p^{\,1/2} \qquad (5.10)$$

For the optimum fit shown in Fig. 11, where Γ_c = 0.35 and $\Phi_{min,EI}$ = 0.335, it follows that, when ΔC_p = 1.55, $C_{d,e,EI}$ = 0.394 and hence $C_{d,i,EI}$ = 0.138. That is, the determination of $\Phi_{min,EI}$ and Γ_c from the fitted effectiveness data implicitly determines the values of $C_{d,e,EI}$ and $C_{d,i,EI}$; the actual values of the discharge coefficients can only be calculated if the value of ΔC_p is known.

Table 2 shows the values of $C_{d,e}$ for the optimum case and for Γ_c = 0.25, 0.5, 0.75 and 1. Having found $\Phi_{min,EI}$ - using the regression analysis described in section 5.3 - $C_{d,e,EI}$ and K were evaluated for each value of Γ_c using eqs (5.10) and (3.3) respectively. It should be noted, however, that these values are all based on ΔC_p = 1.55, which only satisfies the consistency criterion for the Γ_c = 0.35 case. (In principle, it should be possible to find an appropriate value of ΔC_p for some of the other cases but this was not attempted here.) Values of Φ_i*, the maximum value of the nondimensional ingress calculated using eq (5.7), are also included in Table 2.

Γ_c	g*	$\Phi_{min,EI}$	Φ_i*	$C_{d,e,EI}$	K
0.25	0.284	0.396	0.060	0.477	0.450
0.35	**0.332**	**0.335**	**0.064**	**0.394**	**0.371**
0.5	0.386	0.287	0.069	0.345	0.326
0.75	0.452	0.239	0.073	0.288	0.271
1	0.500	0.233	0.082	0.280	0.264

Table 2 Computed parameters for saw-tooth model for ΔC_p = 1.55

(Γ_c = 0.35 is the optimum value.)

Fig. 13 shows the variation of the pressure shape factor *f*, which is defined by eq (3.1), and it can be seen that saw-tooth model provides a reasonable approximation. The computed pressures were evaluated at x = 0.93, y =0, the location used above to evaluate ΔC_p. It is interesting to compare Fig. 13 with Fig. 6, which shows the variation of *f* (at *x* = -1, *y* = 0.1) for the data of Johnson *et al.* [12]. Despite the different locations, and the different values of ΔC_p and Γ_c, there are similarities between the computed profiles.

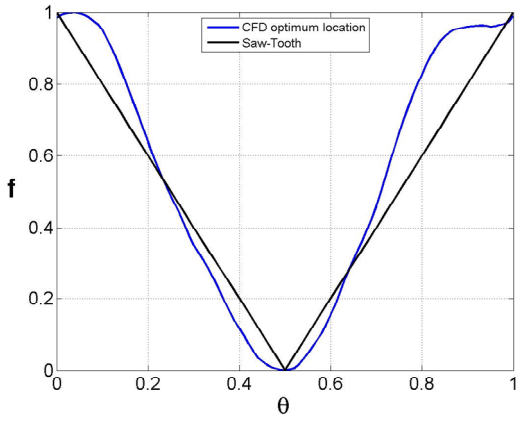

Fig. 13 Computed variation of pressure shape factor *f* with θ inside annulus at x = 0.93, y = 0.

It is also interesting to compare the parameters in Table 2 with those in Table 1 for the data of Johnson *et al.* The differences in $\Phi_{min,EI}$ in these two tables are caused mainly by the differences in the values of ΔC_p. (The vane profile used in the CFD described in Section 4 was chosen to create a large value of this parameter.) Despite the differences in ΔC_p and Γ_c for the results presented here and those discussed in Section 3, the values of $C_{d,e,EI}$ = 0.394 and K = 0.371 for the optimum case in Table 2 are remarkably similar in magnitude to the values in Table 1. Rounded to one-significant-figure, the value of $C_{d,e,EI}$ in Table 2 is the same as that given by Johnson *et al.*

The word 'remarkably' is used above because ΔC_p, $C_{d,e,EI}$ and K depend on where and how they are evaluated. (The similarity between the parameters in Tables 1 and 2 could be fortuitous or it could be because the value of ΔC_p determined from one location in the annulus correlates with the value determined at another location.) It is therefore difficult to compare the values of ΔC_p, $C_{d,e,EI}$ and K obtained in one set of experiments or computations with another. Fortunately, these 'secondary parameters' are unnecessary in the determination of $\Phi_{min,EI}$.

Finally, the computed pressure differences used here can be compared with the limits given by eqs (C8) and (C9) in Appendix C for incompressible flow through the seal. For the CFD solutions, $\Delta p / p$ = 0.062 and $p_{2,max} / p_{2,min}$ = 1.06, which are well within the theoretical limits for incompressible flow. So, despite the fact that compressible flow occurs in the annulus (where $M \approx 0.65$), the incompressible orifice equations are still valid.

6. CONCLUSIONS

Values of the sealing effectiveness determined from the saw-tooth model for externally-induced (EI) ingress have been

compared with published values (Johnson *et al.* [12]) obtained from an experimental rig with stationary vanes and rotating blades in the annulus. In addition, steady 3D CFD was used to compute the effectiveness at several values of the sealing flow rate in the model of an experimental rig with vanes, but no blades, in the annulus. In all cases, axial-clearance seals were used; for the CFD, a thin-seal approximation was used. The principal conclusions are given below.

- EI ingress is caused predominantly by ΔC_p, the nondimensional peak-to-trough pressure difference in the annulus; the *shape* of the pressure distribution in the annulus is of secondary importance for the prediction of ingress.
- The saw-tooth model produced reasonably accurate results for both the experimental and CFD data; a cosine approximation for the pressure distribution was not significantly more accurate than the saw-tooth model and, unlike the saw-tooth, it required numerical rather than analytical solutions of the orifice equations.
- The saw-tooth model provides a simple equation (eq. (5.6)) that expresses ε, the sealing effectiveness, in terms of Φ_o, the nondimensional sealing flow rate. The correlation between this equation and the computed (or measured) values of ε and Φ_o depends on only two empirical parameters: $\Phi_{min,EI}$, the minimum value of Φ_o required to prevent ingress, and Γ_c, the ratio of the discharge coefficients for ingress and egress.
- A regression analysis of the eight computed ε, Φ_o data points showed that the optimum values of $\Phi_{min,EI}$ and Γ_c were 0.335 and 0.35 respectively; these values resulted in a very good fit between the saw-tooth model and the data. (In principle, $\Phi_{min,EI}$ and Γ_c could be estimated using only two data points, but a regression analysis gives improved estimates when more data points are available.)
- Another important advantage of eq (5.6) is that the estimate of $\Phi_{min,EI}$ (from the ε, Φ_o data points) requires no knowledge of the value of ΔC_p (the external pressure coefficient, or the discharge coefficients, or indeed any other parameter in the annulus.
- The computations showed that the value of ΔC_p varied throughout the annulus. Although this parameter is not needed to calculate $\Phi_{min,EI}$, a consistency criterion was proposed for its determination. Using this criterion, the location in the annulus for the determination of ΔC_p was shown to be near the downstream edge of the seal clearance, where $\Delta C_p \approx 1.55$. (This location might not be appropriate in other cases.)
- Although, like ΔC_p, the value of $C_{d,e}$ (the discharge coefficient for egress) is not needed to calculate $\Phi_{min,EI}$, the value of $C_{d,e} \approx 0.4$ found from the CFD data was (perhaps fortuitously) consistent with the values found from the experimental data.
- For the optimum case (where $\Phi_{min,EI}$ = 0.335 and Γ_c = 0.35), the saw-tooth model showed that $\Phi_i^* / \Phi_{min,EI} \approx 0.19$, where Φ_i^* is the ingested flow rate when the sealing flow rate is zero. This result, which corresponds to the maximum ingress (and minimum egress) case, shows that the maximum flow that can be ingested into the wheel-space is approximately 19% of the flow rate needed to seal the system. (This value, which depends on Γ_c, might be inappropriate at other conditions.)
- The criteria for incompressible flow through the seal clearance were quantified for both EI and RI ingress. Although the computed flow in the annulus was compressible (with $M \approx 0.65$ for the CFD computations), it was shown that the incompressible orifice equations were still valid.
- In principle, the value of $\Phi_{min,EI}$ determined using the saw-tooth model in an experimental rig operating at one value of the rotational Reynolds number should apply to a geometrically-similar engine operating at some other value.(This hypothesis has yet to be tested.)

In Part 2 of this two-part paper, the orifice model is applied to the case of combined ingress, where the effects of rotation and external flow are both significant.

ACKNOWLEDGEMENTS

This research was partially funded by the UK EPSRC (EP/G069107/1). We wish to thank the China Scholarship Council and Beihang University, Beijing, China, for supporting Kunyuan Zhou. He conducted his CFD research using the Aquila High Performance Computing facility at the University of Bath. We would also like to thank the reviewers for their helpful comments.

APPENDIX A: SOLUTION OF ORIFICE EQUATIONS FOR EI AND RI INGRESS

The most important results obtained from the orifice equations are summarised below, and definitions of the symbols are given in the Nomenclature. The subscripts 1 and 2 refer respectively to locations in the wheel-space and annulus, and details of the derivations and solutions of the equations are given by Owen [1, 2]. A schematic diagram of the orifice model, on which the equations are based, is shown in Fig. 4.

A1 Orifice equations for EI and RI ingress

The equations, which are valid for both EI and RI ingress, can be expressed as

$$\frac{V_{r,e}}{\Omega b} = C_{d,e}\sqrt{C_{\beta_1} - C_p} \qquad \text{(A1)}$$

when $C_{\beta_1} \geq C_p$, and

$$\frac{V_{r,i}}{\Omega b} = C_{d,i}\sqrt{C_p - C_{\beta_2}} \qquad \text{(A2)}$$

when $C_p \geq C_{\beta_2}$, where

$$C_p = \frac{p_2 - p_1}{1/2\rho\Omega^2 b^2},\ C_{\beta 1} = \beta_1^2\left(1 - \frac{r_1^2}{r_2^2}\right), C_{\beta_2} = \beta_2^2\left(\frac{r_2^2}{r_1^2} - 1\right) \qquad \text{(A3)}$$

The mass flow rates can be calculated by integrating the velocities across the seal clearance, so that

$$\dot{m}_e = \rho \int_{A_e} V_{r,e}\, dA_e \ \ and \ \ \dot{m}_i = \rho \int_{A_i} V_{r,i}\, dA_i \qquad \text{(A4)}$$

The nondimensional superposed flow rate, $C_{w,o}$, which can be calculated using eq (A4), is given by

$$C_{w,o} = C_{w,e} - C_{w,i} \qquad \text{(A5)}$$

The sealing effectiveness, ε, is defined by

$$\varepsilon = 1 - \frac{C_{w,i}}{C_{w,e}} \qquad \text{(A6)}$$

A2 Solution of equations for RI ingress with no external swirl

$$\Phi_{min,RI} = \frac{C_{w,min,RI}}{2\pi G_c\, Re_\phi} = C_{d,e} C_{\beta_1}^{1/2} \qquad \text{(A7)}$$

and

$$\varepsilon_{RI} = \frac{1 - \Gamma_p(1 + \Gamma_c^2)}{1 - \Gamma_p} \qquad \text{(A8)}$$

A3 Solution of equations for EI ingress with no external swirl

It is convenient to define *f*, a shape factor for the circumferential distribution of pressure in the annulus, as

$$f(\theta) = \frac{p_2 - p_{2,min}}{\Delta p} \qquad \text{(A9)}$$

for the range $0 \leq f(\theta) \leq 1$, where $0 \leq \theta \leq 1$ is the relative angular position (between the vanes in an engine), and $\Delta p = p_{2,max} - p_{2,min}$ is the peak-to-trough pressure difference in the annulus. A simplified representation of the circumferential distribution of pressure and radial velocity is shown in Fig. A1.

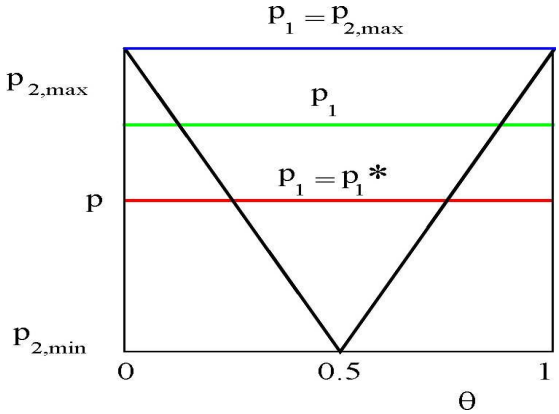

(a) Circumferential distribution of p_1 and p_2

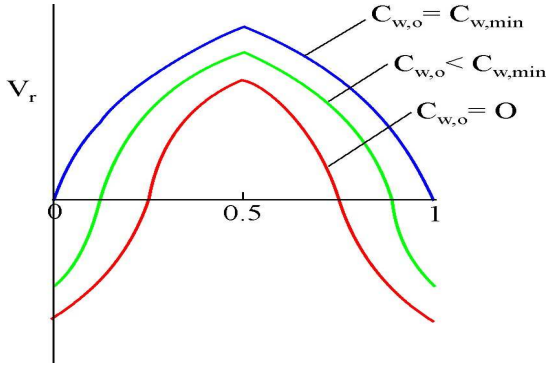

(b) Circumferential distribution of V_r

Fig. A1 Circumferential distribution of pressure and radial velocity for saw-tooth model [2]

It is also convenient to define *g*, a normalised axisymmetric pressure in the wheel-space, as

$$g = \frac{p_1 - p_{2,min}}{\Delta p} \qquad \text{(A10)}$$

for the range $g^* \leq g(p_1) \leq 1$, where g^* is the value of g when $C_{w,0} = 0$.

The solutions of the orifice equations can be written as

$$\Phi_{min,EI} = \frac{C_{w,min,EI}}{2\pi G_c\, Re_\phi} = C_{d,e,EI}\, I_{min} \Delta C_p^{1/2} \qquad \text{(A11)}$$

and

$$\varepsilon_{EI} = 1 - \frac{\Gamma_c I_i}{I_e} \qquad \text{(A12)}$$

where

$$I_{min} = \int_o^1 \{1 - f\}^{1/2}\, d\theta \qquad \text{(A13)}$$

$$I_e = \int_{\theta'}^1 (g - f)^{1/2}\, d\theta \qquad \text{(A14)}$$

$$I_i = \int_0^{\theta'} (f - g)^{1/2}\, d\theta \qquad \text{(A15)}$$

and θ' is the value of θ where $V_r = 0$.

A4 Saw-tooth model for EI ingress

Fig. A1 shows the circumferential distribution of pressure and radial velocity for the saw-tooth model which was used by Owen [2] for $\Gamma_c = 1$.

From the above definitions of *f* and *g*, it is assumed that

$$f = 1 - 2\theta \tag{A16}$$

when $0 \le \theta \le 1/2$ and

$$f = 2\theta - 1 \tag{A17}$$

when $1/2 < \theta \le 1$. It can be shown that

$$I_{min} = \frac{2}{3} \tag{A18}$$

$$\Phi_{min,EI} = \frac{C_{w,min,EI}}{2\pi G_c \, Re_\phi} = \frac{2}{3} C_{d,e} \, \Delta C_p{}^{1/2} \tag{A19}$$

$$\frac{C_{w,e}}{C_{w,min,EI}} = g^{3/2} \tag{A20}$$

$$\frac{C_{w,i}}{C_{w,min,EI}} = \Gamma_c (1-g)^{3/2} \tag{A21}$$

$$\frac{C_{w,0}}{C_{w,min,EI}} = g^{3/2} - \Gamma_c (1-g)^{3/2} \tag{A22}$$

As $g = g^*$ when $C_{w,o} = 0$, it follows from eq (A22) that

$$g^* = \frac{1}{1 + \Gamma_c{}^{-2/3}} \tag{A23}$$

Hence, from eq (A21),

$$\frac{C_{w,i}{}^*}{C_{w,min,EI}} = \frac{1}{(1 + \Gamma_c{}^{-2/3})^{3/2}} \tag{A24}$$

where $C_{w,i}{}^*$ is the maximum ingress, which occurs when $C_{w,o} = 0$.

As

$$\varepsilon = 1 - \frac{C_{w,i}}{C_{w,e}} \tag{A25}$$

it follows that, for $g^* \le g \le 1$,

$$\varepsilon_{EI} = 1 - \Gamma_c \left[\frac{1-g}{g} \right]^{3/2} \tag{A26}$$

APPENDIX B: CONSISTENCY CRITERION FOR DETERMINATION OF ΔC_p

Having found $\Phi_{min,EI}$ and Γ_c using the regression analysis described in Section 5.3, ΔC_p can be determined from the CFD computations in the annulus. As ΔC_p depends on where in the annulus it is evaluated, the position at which to evaluate it is not obvious. (This position is equivalent to the location of station 2 in the annulus, which was used in the derivation of the orifice equations and which is shown diagrammatically in Fig. 4.) For the saw-tooth model, the appropriate position is determined using the 'consistency criterion' described below.

In experiments, ΔC_p is usually evaluated for the case of zero superposed flow, such that $\Phi_o = 0$. For this condition, eq (A23) shows that

$$g = g^* = \frac{1}{1 + \Gamma_c{}^{-2/3}} \tag{B1}$$

where g^* is the value of *g*, the normalised pressure in the wheel space defined by eq (A10). For the optimum value of $\Gamma_c = 0.35$, determined from the regression analysis used in Section 5.3, it follows from eq (B1) that $g^* = 0.332$.

Fig. B1 shows the computed contours of g in the annulus for $\Phi_o = 0$, and it can be seen that $g = g^* = 0.332$ in very restricted regions near the upstream (x = -1) and downstream (x = +1) edges of the seal clearance. (Although p_1 is constant, *g* varies according to eq (A10) as $p_{2,min}$ and $p_{2,max}$, and therefore Δp, vary throughout the annulus.)

The contours of $g = g^* = 0.332$ are the only locations in the annulus where the optimised saw-tooth model is mathematically consistent with the CFD results, and the x-y variation of this g^* contour is referred to below as the 'g* locus'. *For mathematical consistency, ΔC_p should only be evaluated at the x,y locations in the annulus that correspond to this locus.*

Fig. B2 shows a close-up view of the ΔC_p contours computed near the seal clearance, and the dotted line shows the g* locus: the values of ΔC_p that lie on this locus satisfy the consistency criterion. The locus lies inside the mixing region in the annulus, which was referred to in Section 5.3, and there is a very small range for the values of ΔC_p that can be used. It was assumed here that ΔC_p = 1.55, which corresponds to the location (x,y) = (0.93,0), near the downstream edge of the seal clearance.

The consistency criterion is a mathematical construct. In an experiment, it would be virtually impossible to determine the location of the g^* locus as pressure instrumentation is usually located on the inner or outer walls of the annulus. This means that the value of ΔC_p determined experimentally would almost certainly be unable to satisfy the consistency criterion, and the consequent value of $C_{d,e}$ would depend on where ΔC_p was determined. A physical if not mathematical consistency could be achieved by extrapolating data from a rig to an engine, say, if the same relative locations were used in both cases.

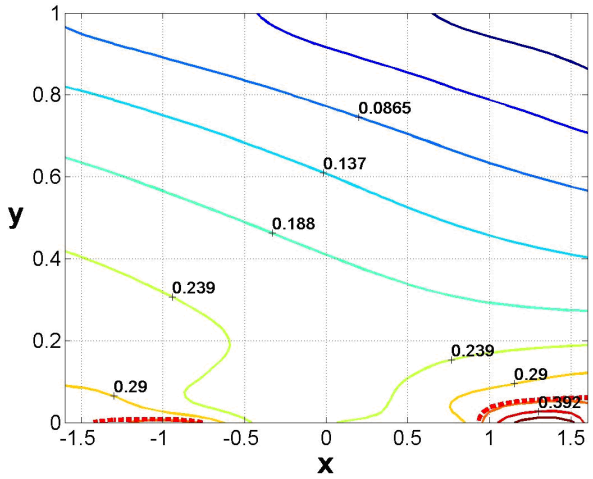

Fig. B1 Contours of nondimensional pressure g computed inside annulus for $\Phi_o = 0$
(Dotted line corresponds to contour of g*= 0.332.)

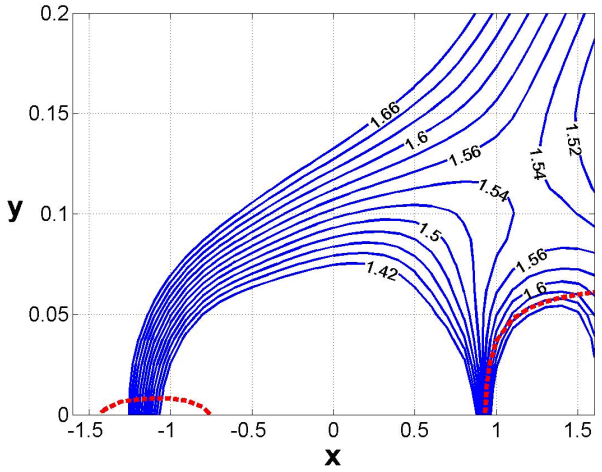

Fig. B2 Close-up of contours of ΔC_p computed near seal clearance for $\Phi_o = 0$. (Dotted line corresponds to locus of g*= 0.332.)

APPENDIX C: LIMITS OF INCOMPRESSIBLE FLOW

C1 Incompressibility criterion

As the flow in the annulus of gas turbines is compressible, it is reasonable to question the assumption that ingress can be treated as incompressible flow.

For isentropic flow of a perfect gas

$$\frac{\rho_o}{\rho} = \left(1 + \frac{\gamma - 1}{2} M^2\right)^{\frac{1}{\gamma - 1}} \qquad \text{(C1)}$$

where ρ_o, ρ are the total and static densities respectively and M is the Mach number. For $M^2 << 1$, it follows that

$$\frac{\rho_o - \rho}{\rho} \approx \frac{1}{2} M^2 \qquad \text{(C2)}$$

so that the difference in density is less than 5% for $M < 0.3$. It is customary to use this value of the Mach number to define the limit of incompressible flow.

The Mach number is defined as

$$M = \frac{V}{c} = \frac{V}{\sqrt{\gamma R T}} = \frac{V}{\sqrt{\gamma\, p / \rho}} \qquad \text{(C3)}$$

where c is the speed of sound. This begs the question: what values of the velocity V and the temperature T are appropriate for ingress? The answer assumed here is that V should be the bulk-average egress velocity corresponding to the maximum value of $C_{w,min}$ and T should be the egress temperature at this condition.

Using the above definition of V,

$$C_{w,min} = 2\pi G_c \frac{\rho b V}{\mu} \qquad \text{(C4)}$$

Separate limits for EI and RI ingress are derived below.

C2 Limit for EI ingress

As the discharge coefficient is unity for isentropic flow, eq (A11) in Appendix A can be written as

$$\Phi_{min,EI} = \frac{C_{w,min,EI}}{2\pi G_c\, Re_\phi} = I_{min} \Delta C_p^{\,1/2} \qquad \text{(C5)}$$

It therefore follows from eq (C3) that

$$M = I_{min} \left(2 \frac{\Delta p}{\gamma p}\right)^{1/2} \qquad \text{(C6)}$$

where $\Delta p = p_{2,max} - p_{2,min}$ is the peak-to-trough circumferential difference in static pressure in the annulus. Hence for air, where $\gamma = 1.4$, and using the saw-tooth model, where $I_{min} = 2/3$,

$$M = 0.797 \left(\frac{\Delta p}{p}\right)^{1/2} \qquad \text{(C7)}$$

If $M < 0.3$ then this implies that

$$\frac{\Delta p}{p} < 0.142 \qquad \text{(C8)}$$

Alternatively, as the pressure in the wheel-space will be $p_{2,max}$ when $C_{w,o} = C_{w,min,EI}$, eq (C8) implies that the incompressible-flow assumption should be valid if

$$\frac{p_{2,max}}{p_{2,min}} < 1.17 \qquad \text{(C9)}$$

It should be noted that, even when the incompressible orifice equations are valid, compressible flow in the annulus means that Δp and ΔC_p will depend on the Mach number.

C3 Limit for RI ingress

The Bayley-Owen correlation (eq (2.1)) is used here, such that

$$\Phi_{min,RI} = \frac{C_{w,min,RI}}{2\pi G_c \, Re_\phi} = 0.097 \qquad \text{(C10)}$$

It therefore follows from eqs (C3) and (C4) that

$$M = 0.097 \frac{\Omega b}{c} \qquad \text{(C11)}$$

For the incompressible- flow assumption to be valid, such that $M < 0.3$, it is necessary that

$$\frac{\Omega b}{c} < 3.1 \qquad \text{(C12)}$$

This limit will never be exceeded for any case of practical importance.

REFERENCES

1. Owen, J.M., 2009, "Prediction of ingestion through turbine rim seals. Part1: Rotationally-induced ingress"; ASME Paper GT2009-59121. To appear in ASME J Turbo.
2. Owen, J.M., 2009, "Prediction of ingestion through turbine rim seals. Part 2: Externally-induced and combined ingress"; ASME Paper GT2009-59122. To appear in ASME J Turbo.
3. Owen, J.M., Pountney, O. and Lock, G.D., 2010, "Prediction of Ingress through Turbine Rim Seals. Part 2: Combined Ingress"; ASME Paper GT2000-23349.
4. Bayley, F. J. and Owen, J., 1970, "The Fluid Dynamics of a Shrouded Disk System with a Radial Outflow of Coolant"; ASME J Eng Power, **92**, pp. 335-341.
5. Graber, D. J., Daniels, W. A. and Johnson, B. V., 1987, "Disk Pumping Test, Final Report"; Air Force Wright Aeronautical Laboratories, Report No. AFWAL-TR-87-2050.
6. Phadke, U.P. and Owen, J.M., 1988, "Aerodynamic Aspects of the Sealing of Gas-Turbine Rotor-Stator Systems, Part 1: The Behaviour of Simple Shrouded Rotating-Disk Systems in a Quiescent Environment"; Int J Heat Fluid Flow, **9**, pp 98-105.
7. Phadke, U.P. and Owen, J.M., 1988, "Aerodynamic Aspects of the Sealing of Gas-Turbine Rotor-Stator Systems, Part 2: The Performance of Simple Seals in a Quasi-Axisymmetric External Flow"; Int J Heat Fluid Flow, **9**, pp 106-112.
8. Phadke, U.P. and Owen, J.M., 1988, "Aerodynamic Aspects of the Sealing of Gas-Turbine Rotor-Stator Systems, Part 3: The Effect of Non-Axisymmetric External Flow on Seal Performance"; Int J Heat Fluid Flow, **9**, pp 113-117.
9. Hamabe, K., and Ishida, K., 1992, "Rim Seal Experiments and Analysis of a Rotor-Stator System with Nonaxisymmetric Main Flow"; ASME Paper 92-GT-160.
10. Chew, J. W., Green, T., and Turner, A. B., 1994, "Rim Sealing of Rotor-Stator Wheel-spaces in the Presence of External Flow"; ASME Paper 94-GT-126.
11. Bohn, D. and Wolff, M., 2003, "Improved Formulation to Determine Minimum Sealing Flow - Cw, min – for Different Sealing Configuration"; ASME Paper GT2003-38465.
12. Johnson, B.V., Jakoby, R., Bohn, D.E., Cunat, D., 2006, "A Method for Estimating the Influence of Time-Dependent Vane and Blade Pressure Fields on Turbine Rim Seal Ingestion"; ASME Paper GT2006-90853.
13. Bohn, D. E., Decker, A., Ma, H., Wolff, M., 2003, "Influence of Sealing Air Mass Flow on the Velocity Distribution in and inside the Rim Seal of the Upstream Cavity of a 1.5-Stage Turbine"; ASME Paper GT2003-38459.
14. Johnson, B.V., Cheng-Zhang Wang and Roy, P.R., 2008, "A Rim Seal Orifice Model with Two Cds and Effect of Swirl in Seals"; ASME Paper GT2008-50650.
15. Laskowski, G. M., Bunker, R. S., Bailey, J. C., Kapetanovic, S., Itzel, G.M., Sullivan, M.A.and Farrell, T.R., 2009, "An Investigation of Turbine Wheelspace Cooling Flow Interactions with a Transonic Hot Gas Path – Part 2: CFD Simulations"; ASME paper GT-2009-59193.
16. M. Rabs, F.-K. Benra, H. J. Dohmen and O. Schneider, 2009, "Investigation of Flow Instabilities near the Rim Cavity of a 1.5 Stage Gas Turbine"; ASME paper GT2009-59965.
17. Zhou, D.W., Roy, R.P., Wang, C.-Z., Glahn, J.A., 2009, "Main Gas Ingestion in a Turbine Stage for Three Rim Cavity Configurations"; ASME paper GT2009-59851.
18. Mirzamoghadam, A.V., Heitland, G., Morris, M.C., Smoke, J., Malak, M. and Howe, J., 2008, "3d CFD Ingestion Evaluation Of a High Pressure Turbine Rim Seal Disk Cavity"; ASME paper GT2008-50531.
19. Mirzamoghadam, A.V., Heitland, G., and Hosseini, K. M. 2009, "The Effect of Annulus Reynolds Number on Rotor-Stator Cavity Sealing Flow"; ASME paper GT2009-59380.
20. Hills, N. J., Chew, J. W., and Turner, A. B.,2002, "Computational and mathematical modeling of turbine rim seal ingestion"; J. Turbo, vol 124:306-315.
21. Lewis, P. R., Wilson, M., 2007, "Three-dimensional computations of ingress in gas turbine cooling systems"; International Gas Turbine Congress, Tokyo, December 2-7, paper TS-040.
22. Zhou, K., Wilson, M., Lock, G.D. and Owen, J.M., 2010, "Computation of Ingestion through Gas Turbine Rim Seals"; to be submitted to ASME J. Turbo.